Table 3.1.2
Run-time parameters used for collection of the data used for certification of SRM 660b

The 'overhead time' associated with the operation of the goniometer is included.

hkl	Start angle (°)	End angle (°)	Step width (°)	Count time (s)	Total peak time (min)
100	20.3	22.2	0.01	2	6.3
110	29.1	31.4	0.01	1	3.8
111	36.4	38.4	0.01	3	10.0
200	42.7	44.4	0.01	5	14.2
210	48	50	0.008	2	8.3
211	53.2	54.896	0.008	5	17.7
110	62.5	64.204	0.008	11	39.0
300	66.7	68.596	0.008	4	15.8
310	70.9	72.7	0.008	6	22.5
311	75	76.904	0.008	9	35.7
222	79.3	80.804	0.008	47	147.3
320	83	84.904	0.008	15	59.5
321	86.9	88.9	0.008	8	33.3
400	95	96.704	0.008	42	149.1
410	98.6	100.8	0.008	9	41.3
330	102.7	104.9	0.008	12	55.0
331	106.9	108.9	0.01	27	90.0
420	111.1	113.1	0.01	20	66.7
421	115.3	117.6	0.01	10	38.3
332	119.9	122.1	0.01	19	69.7
422	129.6	131.796	0.012	32	97.6
500	134.9	137.396	0.012	27	93.6
510	140.5	144	0.014	7	29.2
511	147.5	150.908	0.016	15	53.2
					Total time = 20.0 hours

second involved a simple continuous scan of fixed step width and count time. It is generally accepted that a step width should be chosen so as to collect a minimum of five data points above the full-width-at-half-maximum (FWHM) to obtain data of sufficient quality for a Rietveld analysis (Rietveld, 1967, 1969; McCusker *et al.*, 1999). This does not, however, constitute any sort of threshold; collecting data of a finer step width can, with proper data analysis, result in a superior characterization of the IPF. However, one must consider the angular range of acceptance of the receiving slit that is chosen. For a slit of 0.05° a step width of 0.005° would add only 10% 'new' information, so selecting this step width would not be worth the extra data-collection time. We did, however, collect some data sets we refer to as 'ultra-high-quality' data; the step widths for these were half those shown in Table 3.1.2 and the count times were approximately three times higher than those in Table 3.1.2. For the reported instrument and configuration, the run-time parameters of Table 3.1.2 result in a minimum of 8 to 10 points above the FWHM. Count times were selected to obtain a uniform number of counts for each profile. It should be noted that it is probably not worth spending time collecting quality data from the 222 line of LaB_6, as it is of low intensity and relatively close to other lines of higher intensity; however, this is not the case with the 400 line. Selection of the run-time parameters can be an iterative process; the total width of each profile scan was set to include at least 0.3° 2θ of apparent background on either side of the profile. Except for the data for SRM 676a, the continuous scans discussed were collected with a step width of 0.008° 2θ and a count time of 4 s to result in a scan time of roughly 24 h. The scans of 676a were collected with 0.01° 2θ step width and 5 s count time.

The PSD used on the NIST diffractometer was a one-dimensional silicon strip detector operated in picture-taking mode for all data collection. It has an active window length of 14.4 mm that is divided into 192 strips for a resolution of 75 μm. With a goniometer radius of 217.5 mm this constitutes an active angular range of 3.80° with 0.020° per strip. Slits that would limit the angular range of the PSD window were not used; with each step the counts from all 192 channels were recorded. The PSD was stepped at 0.005° 2θ, for 25% new information per strip; however, to reduce the data-collection time a second coarse step was also included. Therefore, the data-collection algorithm includes the selection of three parameters: a fine step of 0.005°, the number of fine steps between coarse steps (4), and the size of a coarse step (typically 0.1° or 0.2° 2θ). This approach allows for the collection of high-resolution data without stepping through the entire pattern at the high-resolution setting. Data were collected with four fine steps per detector pixel and a coarse step of 0.1° 2θ. They were processed to generate x–y data for subsequent analysis. The operator can select the portion of the 192 channels, centred in the detector window, to be included in the generation of the x–y file. The PSD was fitted with a 1.5° Soller slit for collection of the data presented here.

3.1.5. Data-analysis methods

Data-analysis procedures can range from the entirely non-physical, using arbitrary analytical functions that have been observed to yield reasonable fits to the observation, to those that exclusively use model functions, derived to specifically represent the effect of some physical aspect of the experiment. The non-physical methods serve to parameterize the performance of the instrument in a descriptive manner. The origins of two of the most common measures of instrument performance are illustrated in Fig. 3.1.25. The first is the difference between the apparent position, in 2θ, of the profile maximum and the position of the Bragg reflection computed from the certified lattice parameter. These data are plotted *versus* 2θ to yield a $\Delta(2\theta)$ curve; a typical example is shown in Fig. 3.1.26. An illustration of the half-width-at-half-maximum (HWHM), which is defined as the width of either the right or left half of the profile at one half the value of maximum intensity after background subtraction, is also shown in Fig. 3.1.25. These values can be summed to yield the FWHM, and plotted *versus* 2θ to yield an indication of the profile breadth as it varies with 2θ (Fig. 3.1.27). In addition, the left and right HWHM values of Fig. 3.1.28 gauge the variation of profile asymmetry with 2θ; additional parameters of interest, such as the degree of Lorentzian and Gaussian contribution to profile shape,

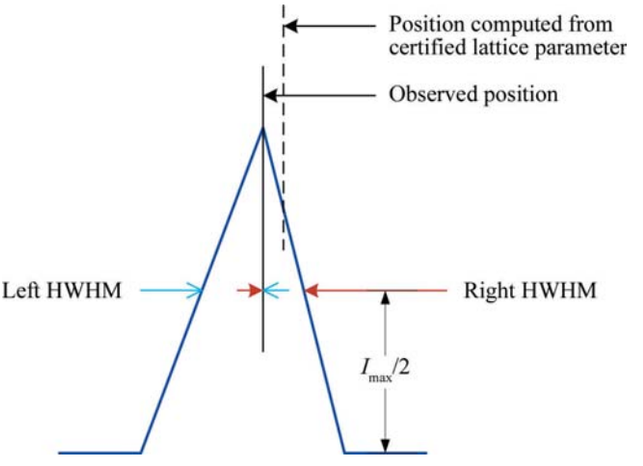

Figure 3.1.25
Diagrammatic representation of a powder-diffraction line profile, illustrating the metrics $\Delta(2\theta)$ and half-width-at-half-maximum (HWHM). The full-width-at-half-maximum (FWHM) = left HWHM + right HWHM.

Copyright © 2018 International Union of Crystallography

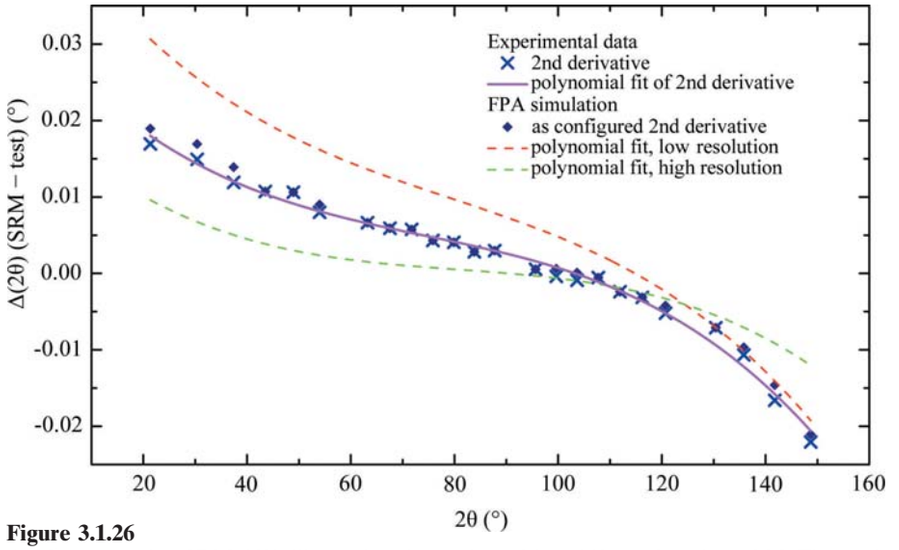

Figure 3.1.26
$\Delta(2\theta)$ curve using SRM 660b illustrating the peak-position shifts as function of 2θ. The peak positions were determined *via* a second-derivative algorithm, and $\Delta(2\theta)$ values (SRM − test) were fitted with a third-order polynomial. Simulated data are from *FPAPC* and were analysed *via* the second-derivative algorithm and polynomial fits as per the experimental data.

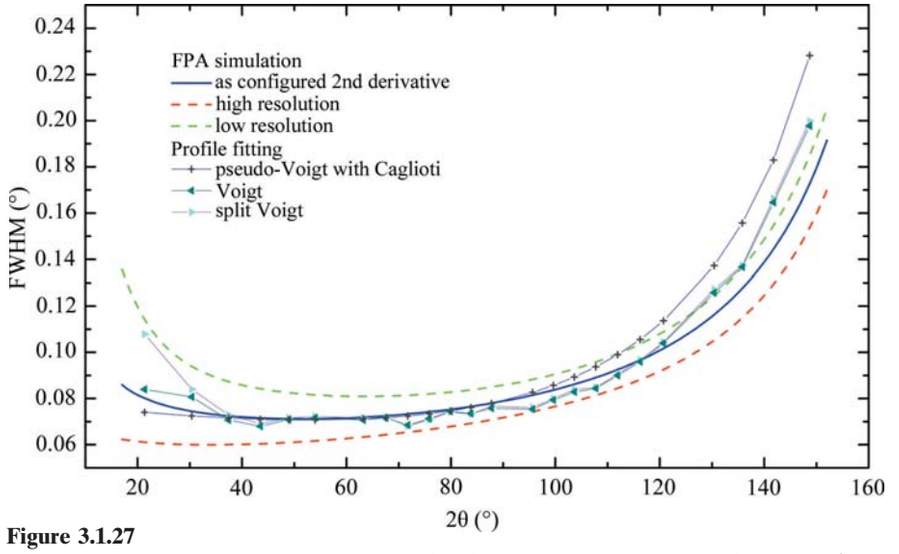

Figure 3.1.27
Simulated and actual FWHM data from SRM 660b using the two Voigt PSFs with ('with Caglioti') and without constraints.

can be plotted *versus* 2θ to describe the instrument and evaluate its performance.

The least computationally intensive methods for the analysis of XRPD data, which have been available since the onset of automated powder diffraction, are based on first- or second-derivative algorithms. These methods report peak positions as the 2θ value at which a local maximum in diffraction intensity is detected in the raw data. Typical software provides 'tuning' parameters so that the operation of these algorithms can be optimized for the noise level, step width and profile width of the raw data. These methods are highly mature and offer a quick and reliable means of analysing data in a manner suitable for qualitative analysis and lattice-parameter refinement. However, they only give information about the position of the top of the peak. Calibration of the diffractometer *via* this method is useful only for subsequent analyses that also use such peak-location methods.

Profile fitting with an analytical profile-shape function offers the potential for greater accuracy, because the entire profile is used in the analysis. As with the derivative-based methods, profile fitting also reports the observed 2θ position of maximum intensity, in addition to parameters describing profile shape and breadth. The discussion of the IPF in Section 3.1.1, as well as a quick look at Figs. 3.1.26–3.1.28, shows the complexity in the line profile shape from a Bragg–Brentano instrument. The profiles are symmetric only in a limited region of 2θ; in other regions, the degree and direction of profile asymmetry also vary as a function of 2θ. To a first approximation, the optics of an instrument contribute to the Gaussian nature of the profiles; this Gaussian nature will be constant with respect to 2θ. The Lorentzian contribution is primarily from the emission spectrum; given the dominance of angular-dispersion effects at high angle, one can expect to see an increase in the Lorentzian character of the profiles with increasing 2θ. While it can be argued that it is physically valid to model specific contributions to the IPF with Gaussian and Lorentzian PSFs, either of these two analytical functions alone cannot be expected to fit the complexities of the IPF and yield useful results. Combinations of these two functions, however, using shape parameters that vary as a function of 2θ, have given credible results for fitting of data from the Bragg–Brentano diffractometer and have been widely incorporated into Rietveld structure-refinement software. The Voigt function is a convolution of a Gaussian with a Lorentzian, while the pseudo-Voigt is the sum of the two. The parameters that are refined consist of an FWHM and shape parameter that indicates the ratio of the Gaussian to Lorentzian character. The Voigt, being a true convolution, is the more desirable PSF as it is more physically realistic; the pseudo-Voigt tends to be favoured as it is less computationally intensive and the differences between the two PSFs have been demonstrated to be minimal (Hastings *et al.*, 1984), although there is not universal agreement about this.

Refining the profile shapes independently invariably leads to errors when analysing patterns with peak overlap, as correlations

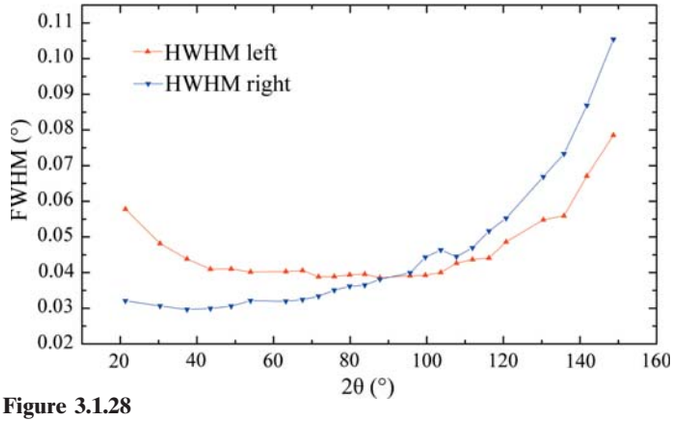

Figure 3.1.28
Left and right HWHM data from SRM 660b using the split pseudo-Voigt PSF fitted with uniform weighting.

occur between shape parameters of neighbouring profiles. This problem can be addressed by constraining the shape parameters to follow some functional form with respect to 2θ. Caglioti *et al.* (1958) developed such a function specifically for constant-wavelength neutron powder diffractometers; it has been incorporated in many Rietveld codes for use with XRPD data. It constrains the FWHM of the Gaussian contribution to the Voigt or pseudo-Voigt PSF:

$$\mathrm{FWHM}^2 = U\tan^2\theta + V\tan\theta + W, \qquad (3.1.1)$$

where the refineable parameters are U, V and W. The term U can be seen to correspond with microstrain broadening from the sample, and broadening due to the angular-dispersion component of the IPF. In *GSAS* an additional term, GP, in $1/\cos\theta$, is included to account for Gaussian size broadening. The Lorentzian FWHM in *GSAS* can vary as

$$\mathrm{FWHM} = \frac{LX}{\cos\theta} + LY\tan\theta, \qquad (3.1.2)$$

where LX and LY are the refineable parameters. Here LX varies with size broadening while LY is the Lorentzian microstrain and angular-dispersion term. Given that the emission spectrum is described with Lorentzian profiles, we would expect the LY term to model the effects of angular dispersion. Within the code *HighScore Plus*, the Lorentzian contribution is allowed to vary as

$$\mathrm{FWHM} = \gamma_1 + \gamma_2(2\theta) + \gamma_3(2\theta)^2, \qquad (3.1.3)$$

where γ_1, γ_2, and γ_3 are the refineable parameters. Alternatives to the Caglioti function have been proposed that are arguably more appropriate for describing the FWHM data from a Bragg–Brentano instrument (Louër & Langford, 1988; Cheary & Cline, 1995). However, they have not yet been incorporated into many computer codes.

The asymmetry in the observed profiles can be fitted with the use of a split profile, where the two sides of the PSF are refined with independent shape and HWHM parameters. This approach will improve the quality of the fit to the observations; however, it is empirical in nature. The more physically valid approach is the use of models to account for the origins of profile asymmetry. The Finger *et al.* (1994) model for axial divergence has been widely implemented in various Rietveld codes. It is formulated to model the axial-divergence effects of a synchrotron powder diffraction experiment where the incident beam is essentially parallel. The two refineable parameters, S/L and H/L, refer to the ratios of sample and receiving-slit length, relative to the goniometer radius; they define the level of axial divergence in the diffracted beam. This model is not in precise correspondence with the optics of a Bragg–Brentano diffractometer where both the incident and diffracted beams exhibit divergence in the axial direction. It does, however, give quality fits to such data. The use of such a model, as opposed to the sole use of a symmetric or split PSF, will yield peak positions and/or lattice parameters that are 'corrected' for the effects of the aberration in question. Therefore, results from the use of model(s) cannot be directly compared with empirical methods that simply characterize the form of the observation. In the case of the Bragg–Brentano experiment, the correction that the Finger model applies is not rigorously correct. However, the impact of axial divergence, regardless of the details of diffractometer optics, is universal; as such the use of the Finger model results in a more accurate assessment of 'true' peak position and, therefore, lattice parameters.

A third PSF that is in common use is the Pearson VII, or split Pearson VII, that was proposed by Hall *et al.* (1977) for fitting X-ray line profiles. No *a priori* physical justification exists for the use of this PSF. The refineable parameters are the FWHM, or HWHM, and an exponent, m. The exponent can range from 1, approximating a Lorentzian PSF, to infinity, where the function tends to a Gaussian. Owing to the lack of a clear physical justification for use of this PSF, it is not often used in Rietveld analysis software.

Convolution-based profile fitting, as shown in Fig. 3.1.4, was proposed by Klug and Alexander in 1954 (see Klug & Alexander, 1974) and much of the formalism of the aberration functions shown in Table 3.1.1 was developed by Wilson (1963). However, limitations in computing capability largely prevented the realization of the full fundamental-parameters approach method until 1992, with the work of Cheary & Coelho. This was made available to the community through the public-domain programs *Xfit*, and later *KoalaRiet* (Cheary & Coelho, 1996) and more recently *via TOPAS*. Other FPA programs are available, most notably *BGMN* (Bergman *et al.*, 1998); more recently, *PDXL 2* has had some FPA models incorporated. Within the FPA there are no PSFs other than the Lorentzians used to describe the emission spectrum, the shapes of which are not typically refined. All other aspects of the observation are characterized with the use of model functions that yield parameters descriptive of the experiment. Plausibility of the analysis is determined through evaluation of these parameters with respect to known or expected values. Direct comparison of the results from an FPA to those from methods using analytical PSFs is difficult because of the fundamental difference in the output from the techniques; for example, FWHM values are not obtained directly from the FPA method. However, the NIST program *FPAPC* can be used to determine FWHM values numerically.

The FPA models of *TOPAS*, *BGMN* and *PDXL 2* were developed specifically for the analysis of data from a laboratory diffractometer of Bragg–Brentano geometry. Analyses using this method would be expected to result in the lowest possible residual error terms that characterize the difference between calculation and observation. As has been discussed, the various aberrations affecting the diffraction line shape are such that the observed profile maxima do not necessarily correspond to the d-spacing of the diffracting plane (hkl), except perhaps in a limited region of 2θ, emphasizing the need for physically valid modelling of the observed line shape to realize a credible value for the lattice parameter. At NIST, we are particularly interested in the capabilities of the FPA method, as one of the primary interests of the NIST X-ray metrology program is obtaining the correct values for lattice parameters. Furthermore, experience has demonstrated that the refined parameters obtained through the use of FPA models can be used in a 'feedback loop' to isolate problems and anomalies with the equipment.

The instrument response, *i.e.* the diffracted intensity as a function of 2θ, is measured by Rietveld analysis using models for intensity-sensitive parameters such as crystal-structure parameters and Lorentz–polarization factors. The extraction of plausible crystal-structure parameters from standards *via* a Rietveld analysis serves as an effective and independently verifiable means of calibrating instrument performance. Considering these refined values provides an effective way to detect defects that vary smoothly over the full range of 2θ. However, errors that are only observable within limited regions of 2θ may be difficult to detect with a whole-pattern method; these should be investigated with second-derivative or profile-fitting methods. SRM

676a (alumina) is well suited to assessing instrument response because it is non-orienting and of high purity. Alumina is of lower symmetry than either silicon or lanthanum hexaboride; it has a considerable number of diffraction lines and has well established structure parameters. A Rietveld analysis of SRM 660c, however, yields the IPF in terms of code-specific profile shape terms and verifies that peak-position-specific aspects of the equipment and analysis are working correctly.

The instrument response may be evaluated with the more conventional data-analysis methods with use of SRM 1976b. Measurements of peak intensities are obtained from the test instrument, typically by profile fitting, and compared with the certified values. However, the use of SRM 1976b with diffraction equipment with different optical configurations may require the application of a bias to the certified values to render them appropriate for the machine to be qualified. This bias is needed to account for differences in the polarization effects from the presence, absence and character of crystal monochromators. The polarization factor for a diffractometer that is not equipped with a monochromator is (Guinier, 1994)

$$\frac{1+\cos^2 2\theta}{2}. \tag{3.1.4}$$

The polarization factor for a diffractometer equipped with only an incident-beam monochromator is (Azároff, 1955)

$$\frac{1+\cos^2 2\theta_m \cos^2 2\theta}{1+\cos^2 2\theta_m}, \tag{3.1.5}$$

where $2\theta_m$ is the 2θ angle of diffraction for the monochromator crystal. The polarization factor for a diffractometer equipped with only a diffracted-beam post-monochromator is (Yao & Jinno, 1982)

$$\frac{1+\cos^2 2\theta_m \cos^2 2\theta}{2}, \tag{3.1.6}$$

where $2\theta_m$ is the 2θ angle of the monochromator crystal. Equations (3.1.5) and (3.1.6) are appropriate when the crystal has an ideal mosaic structure, *i.e.* the diffracting domains are uniformly small and, therefore, the crystal is diffracting in the kinematic limit. This is in contrast to a 'perfect' crystal, which would diffract in accordance with dynamical scattering theory. Note that equations (3.1.5) and (3.1.6) both have the $\cos^2 2\theta_m$ multiplier operating on the $\cos^2 2\theta$ term. Since this multiplier is less than unity, the intensity change on machines equipped with a monochromator exhibits a weaker angular dependence.

The certification data for SRM 1976b were collected with the NIST machine equipped with the Johansson IBM and a scintillation detector. The simplified IPF of this machine is advantageous for the accurate fitting of the profiles and, therefore, intensity measurement. The validity of the 'ideal mosaic' assumption embodied in equation (3.1.5) was evaluated using this diffractometer; the validity of equation (3.1.6) was evaluated with data from the machine configured with the post-monochromator. With respect to equation (3.1.5), for a Ge crystal (111) reflection, $2\theta_m$ was set to 27.3°; with regard to equation (3.1.6), for a pyrolytic graphite crystal (0002) basal-plane reflection, $2\theta_m$ was set to 26.6°. Rietveld analyses of data from SRMs 660b, 1976b and 676a included a refinement of the polarization factor, modelled according to equations (3.1.5) and (3.1.6) in *TOPAS*, and yielded fits of high quality, indicating that these models were appropriate for these crystals and configurations. Equations (3.1.4), (3.1.5) and (3.1.6) were used to bias the certified values to correspond to those of alternative configurations. These values are included in the SRM 1976b CoA as ancillary data.

3.1.6. Instrument calibration

The calibration procedure has traditionally involved the comparison of measurements from a reference (an SRM) with those of the test instrument. However, the exact form of this comparison depends upon the data-analysis procedure to be used. A classical calibration, permitting qualitative analyses and lattice-parameter refinement, can be readily performed as per Fig. 3.1.26. These data are fitted with a polynomial that describes the 2θ error correction that is then applied to subsequent unknown samples. Furthermore, with this calibration method, the actual form of the curve of Fig. 3.1.26 is largely irrelevant. As the data-analysis methods become more advanced, physical models are chosen to replace analytical PSFs. The calibration is then based upon the observation that the machine performance does indeed correspond to the models used, and that acceptable values for refined parameters describing the experiment are obtained from an analysis of data from an SRM. A systematic approach to instrument calibration with a full evaluation of the data, including those obtained from the empirical methods shown in Figs. 3.1.26 and 3.1.27, results in the ability to use the advanced methods in a rational manner and obtain results in which one can have confidence. The advanced methods, while more complex to use and requiring a much more extensive instrument calibration process, reward the user with a sample characterization of greater breadth and reduced measurement uncertainty.

Consider the $\Delta(2\theta)$ curve illustrated in Fig. 3.1.26. The *y*-axis values are the differences between the peak positions computed from the certified lattice parameter of SRM 660b and those of each observed profile determined *via* a second-derivative-based peak-location algorithm. Therefore, each of the $\Delta(2\theta)$ data points plotted on Fig. 3.1.26 were determined independently. It is immediately apparent that the data follow a smooth, monotonic curve with no substantive outliers. Discontinuities or non-monotonicity would typically indicate mechanical difficulties with the equipment, such as loose components or problems with the goniometer assembly. Evaluation of independently determined data such as these is critical to verifying that there are no 'high-frequency' difficulties with the equipment that would otherwise be hidden or smoothed out with the use of methods that apply models or constraints across the entire 2θ range, such as a Rietveld analysis. The $\Delta(2\theta)$ values were fitted with a third-order polynomial that is also illustrated in Fig. 3.1.26. Consideration of the deviation values between the observations and the third-order fit indicates a random or 'top hat' distribution with a maximum excursion of $\pm 0.0025°$ 2θ; this provides further evidence that a machine is operating properly.

FPAPC was used to generate simulated data, which were then analysed using the same second-derivative algorithm as was applied to the raw data. The aforementioned optical setup of the NIST instrument was used in the as-configured simulation (see the caption for Fig. 3.1.26), while the high-resolution and low-resolution data were simulated with a 50% increase or decrease of the incident and Soller slit angles. For the 'high-resolution' and 'low-resolution' data, third-order polynomial fits to the $\Delta(2\theta)$ values are displayed in Fig. 3.1.26; for the 'as-configured' data, the Δ values themselves are indicated. The correspondence between the simulation and observation indicates that trends in the data can be readily explained in the context of the aberration functions discussed in Section 3.1.1 and that such a machine can